Tellus
SERIES A
DYNAMIC
METEOROLOGY
AND OCEANOGRAPHY
PUBLISHED BY THE INTERNATIONAL METEOROLOGICAL INSTITUTE IN STOCKHOLM

The Lorenz energy cycle: trends and the impact of modes of climate variability

By QIYUN MA[1,2], VALERIO LEMBO[3], and CHRISTIAN L.E. FRANZKE[4,5,6]*, [1]*School of Integrated Climate System Science, University of Hamburg, Hamburg, Germany;* [2]*Meteorological Institute, University of Hamburg, Hamburg, Germany;* [3]*Institute of Atmospheric Sciences and Climate, National Research Council, Bologna, Italy;* [4]*School of Engineering and Science, Jacobs University, Bremen, Germany;* [5]*Institute of Oceanography, University of Hamburg, Hamburg, Germany;* [6]*Center for Climate Physics, Institute for Basic Science, Pusan National University, Busan, Republic of Korea*

(Manuscript Received 25 December 2020; in final form 24 February 2021)

ABSTRACT

The atmospheric circulation is driven by heat transport from the tropics to the polar regions, embedding energy conversions between available potential and kinetic energy through various mechanisms. The processes of energy transformations related to the dynamics of the atmosphere can be quantitatively investigated through the Lorenz energy cycle formalism. Here we examine these variations and the impacts of modes of climate variability on the Lorenz energy cycle by using reanalysis data from the Japanese Meteorological Agency (JRA-55). We show that the atmospheric circulation is overall becoming more energetic and efficient. For instance, we find a statistically significant trend in the eddy available potential energy, especially in the transient eddy available potential energy in the Southern Hemisphere. We find significant trends in the conversion rates between zonal available potential and kinetic energy, consistent with an expansion of the Hadley cell, and in the conversion rates between eddy available potential and kinetic energy, suggesting an increase in mid-latitudinal baroclinic instability. We also show that planetary-scale waves dominate the stationary eddy energy, while synoptic-scale waves dominate the transient eddy energy with a significant increasing trend. Our results suggest that interannual variability of the Lorenz energy cycle is determined by modes of climate variability. We find that significant global and hemispheric energy fluctuations are caused by the El Nino-Southern Oscillation, the Arctic Oscillation, the Southern Annular Mode, and the meridional temperature gradient over the Southern Hemisphere.

Keywords: Lorenz energy cycle, climate variability, trends

1. Introduction

The inhomogeneous absorption of energy in the climate system is the primary fuel of atmospheric and oceanic dynamics. Energy is transformed within the system through several forms, following the motion of the atmosphere and the ocean, determining the mean state and variability of the climate system (Hu et al., 2004; Clément et al., 2017). The seminal work by Lorenz (1955) laid down a comprehensive picture of the various processes responsible for the conversion of available potential energy from inhomogeneous diabatic heating into kinetic energy and eventually (frictional) dissipation. This is commonly referred to as the "Lorenz energy cycle", describing the conversion of energies through different forms and treating the system as a thermodynamic cycle or, in our context, as a heat engine.

The atmospheric process of the Lorenz energy cycle can be described as follows: The zonal available potential energy is determined by the net heating of the atmosphere in low latitudes and the net cooling in high latitudes (Ulbrich and Speth, 1991). Then the energy cycle involved in the atmospheric general circulation experiences two main processes: baroclinic growth and barotropic decay (Ulbrich and Speth, 1991; Lembo et al., 2019a). The process of baroclinic growth occurs mainly due to the growth of mid-latitudinal baroclinic eddies at the synoptic scale, including the transformation of the zonal available potential energy into eddy available potential energy through

*Corresponding author. e-mail: christian.franzke@gmail.com

This is an Open Access article distributed under the terms of the Creative Commons Attribution-NonCommercial License (http://creativecommons.org/licenses/by-nc/4.0/), which permits unrestricted non-commercial use, distribution, and reproduction in any medium, provided the original work is properly cited.

Citation: Tellus A: 2021, **73**, 1900033, https://doi.org/10.1080/16000870.2021.1900033

horizontal and vertical transport of sensible heat, and the transformation of eddy available potential energy into eddy kinetic energy by rising warm air and sinking cold air. The energies undergo a process of barotropic decay when a large part of eddy kinetic energy is dissipated by frictional heating and the remainder is converted back into zonal kinetic energy through horizontal and vertical transport of angular momentum by the eddies. This barotropic decay process ensures the maintenance of the extratropical jet streams and storm tracks (Ulbrich and Speth, 1991; Li et al., 2007; Lembo et al., 2019a), however, it is not the leading-order process for the subtropical jet which is mainly due to angular momentum conservation. Finally, the zonal mean meridional overturning circulation leads to the zonal available potential energy converted into zonal kinetic energy, which involves the combined actions of the Hadley and Ferrel cells (Hernández-Deckers and von Storch, 2010; Kim and Kim, 2013).

The Lorenz energy cycle has been widely used to investigate atmospheric dynamics and the general circulation of the atmosphere by considering the physical processes involved in the energy transformation (Peixóto and Oort, 1974; Ulbrich and Speth, 1991, and references therein). By systematically identifying the path through which the atmosphere contributes to achieving a statistically non-equilibrium steady state of the climate system (Ambaum, 2010; Lucarini et al., 2011), the Lorenz energy cycle allows to conveniently describe the climate in the framework of macroscopic non-linear thermodynamics (Prigogine, 1962). In other words, once concepts borrowed from classical thermodynamics, such as efficiency, irreversibility, mechanical work are adapted to the context of the Lorenz energy cycle, a set of metrics is readily available for systematically addressing the maintenance of the mean state and of the variability of the climate system (Lembo et al., 2019a).

The atmospheric Lorenz energy cycle has been evaluated in reanalysis datasets (Li et al., 2007; Kim and Kim, 2013; Pan et al., 2017), and has been used to assess climate model performance (Marques et al., 2009; Hernández-Deckers and von Storch, 2010; Lucarini et al., 2011; Lembo et al., 2019a). Previous studies mainly focused on the mean state and the seasonal cycle of the Lorenz energy cycle. For instance, Hu et al. (2004) examined the Northern Hemisphere atmospheric energetics based on the Lorenz energy cycle framework, using reanalysis data. Marques et al. (2010) focussed on the comparison of different reanalysis datasets in computing the Lorenz energy cycle from 1979 to 2001 while they did not analyse its trends. Pan et al. (2017) first explored the linear trends of various Lorenz energy cycle's components during the period 1979–2013 and compared two reanalysis datasets (ERA-Interim and NCEP-R2). However, trends and the variability of the Lorenz energy cycle as a whole have not been studied widely. A systematic characterisation of these changes provides insight into the impact of anthropogenic global warming, not only in terms of how it affects the efficiency of energy conversions within the atmosphere but also corresponding long-term trends of the atmospheric general circulation (Kim and Kim, 2013; Lembo et al., 2019a).

Here, we systematically examine the variability and trends in the Lorenz energy cycle components over the period 1979–2019. We believe that, for the first time, an extensive focus on long-term variations in Lorenz energy cycle components is provided here. The fluctuations of eddy activities have a major impact on synoptic-scale weather systems, e.g. cyclone and anticyclone systems in mid-latitudes (Pan et al., 2017). Therefore, we will investigate the variations of the Lorenz energy cycle by breaking down the contributions from the eddies into their stationary and transient components. Waves at different scales might contribute differently to the weather and climate variability by transferring heat and momentum fluxes (Lembo et al., 2019b; Chemke and Ming, 2020). We will thus separately examine the Lorenz energy cycle components for different zonal wavenumber regimes as well. We will then relate variations of the Lorenz energy cycle components to key modes of climate variability, investigating the physical processes lying behind such variability from the point of view of climate variability.

In section 2 we describe the data and the Lorenz energy cycle methodology, in section 3 we present our results with a focus on trends in global energies, the energetics of stationary, transient eddies and wavenumber regimes and also the impact of modes of climate variability on energetics. In section 4 we provide our conclusions.

2. Data and methodology

We use reanalysis data provided by the Japan Meteorological Agency (JRA-55) (Kobayashi et al., 2015) to compute the Lorenz energy cycle during the period 1958–2019. The JRA-55 provides 6-hourly data for 37 pressure levels with a 1.25° horizontal resolution. The variables used in computing the Lorenz energy cycle include 3-dimensional fields of daily air temperature, zonal, meridional and vertical winds on pressure levels, and also 2-dimensional daily air temperature, zonal and meridional winds at 2 meters.

We employ the Thermodynamic Diagnostic Tool (TheDiaTo; Lembo et al. (2019a)) for diagnosing the variations of the Lorenz energy cycle (https://github.com/ValerioLembo/TheDiaTo_v1.0.git). The Lorenz energy cycle computations in TheDiaTo allow us to

systematically investigate the energy exchanges embedded in the general circulation of the atmosphere across different spatial scales of motion. This tool is ideal for our purpose to analyze the trends of various components in the Lorenz energy cycle. TheDiaTo subsets and calculates the integrated Lorenz energy cycle in the troposphere between the vertical levels of 900 and 100 hPa. Details of the equations that have been used can be found in Lembo et al. (2019a).

We calculate the following terms in the Lorenz energy cycle: zonal available potential energy P_M, eddy available potential energy P_E, zonal kinetic energy K_M, and eddy kinetic energy K_E. Then, we compute the conversion rates: between zonal and eddy available potential energies $C(P_M, P_E)$, between eddy available potential energy and kinetic energy $C(P_E, K_E)$, between eddy and mean kinetic energies $C(K_E, K_M)$, and between mean available potential energy and kinetic energy $C(P_M, K_M)$, the generation rate of zonal and eddy available potential energies $G(P_M)$ and $G(P_E)$ respectively, and the dissipation rate of zonal and eddy kinetic energies $D(K_M)$ and $D(K_E)$ respectively. Moreover, following Ulbrich and Speth (1991), we decompose the eddy energies in the Lorenz energy cycle into a stationary (subscript SE) and a transient (subscript TE) component. The stationary component is defined as the deviation from the zonal mean, while the transient component is defined as the deviation from the climatological time mean. In doing so, P_E is divided into stationary and transient eddy available potential energies P_{SE} and P_{TE}, and K_E is divided into stationary and transient eddy kinetic energy energies K_{SE} and K_{TE}, respectively. Similarly, we calculate the conversion rates $C(P_M, P_{SE})$, $C(P_M, P_{TE})$, $C(P_{TE}, K_{TE})$, $C(P_{SE}, K_{SE})$, $C(K_{TE}, K_M)$, $C(K_{SE}, K_M)$, two non-linear conversion rates $C(P_{SE}, P_{TE})$ and $C(K_{TE}, K_{SE})$, the generation rates $G(P_{SE})$ and $G(P_{TE})$, and dissipation rates $D(K_{SE})$ and $D(K_{TE})$.

Then we decompose stationary and transient eddy energies into different zonal wave number groups: planetary-scale waves (PW, zonal wave-number 1–3), synoptic-scale waves (SW, wave-number 4–9), and meso-scale waves (MW, wave-number 10–21). This will help us to understand the contributions to the Lorenz energy cycle of different wave number groups representing different weather regimes, from the planetary circulation to regional storms (e.g. Hu et al., 2004; Lembo et al., 2019b; Ruggieri et al., 2020). In this article, we focus only on the decomposition of eddy available potential and eddy kinetic energies on global and hemispheric scales and do not consider the contribution of single wave numbers.

We use the non-parametric Mann–Kendall test to examine the trends for different components of the Lorenz energy cycle and Sen's slope to estimate the magnitude of the trends (Mann, 1945; Sen, 1968; Gocic and Trajkovic, 2013; Franzke and Torelló i Sentelles, 2020). The Mann-Kendall test and Sen's slope are performed using the software MAKESENS (Salmi, 2002).

Three types of climate indices representing modes of climate variability are used in this study: atmospheric indices, oceanic indices, and temperature indices. The atmospheric indices include teleconnection patterns (Feldstein and Franzke, 2017; Hannachi et al., 2017) such as the Arctic Oscillation (AO), the North Atlantic Oscillation (NAO), the Pacific North American (PNA) pattern, the Southern Annular Mode (SAM), and the Quasi-biennial Oscillation (QBO) index. The oceanic indices consist of the El Niño-Southern Oscillation index (NINO3.4), the Pacific Decadal Oscillation (PDO), and the Atlantic Multi-decadal Oscillation (AMO) index. Temperature indices are the monthly HadCRUT4 global mean surface temperature (*GMST*) anomaly and the weighted vertically average (900–100 hPa) meridional temperature difference from JRA-55 (ΔT) at hemispheric-scale. These monthly indices can be downloaded from the website https://climexp.knmi.nl/, except for ΔT. We define the ΔT by calculating the differences between the weighted vertical averaged temperature over the mid-latitudes (30°−60° N/S) and the polar areas (60°–90° N/S). Thus, ΔT_{NH} and ΔT_{SH} depict meridional temperature gradients in the troposphere over the Northern and Southern Hemispheres.

3. Results

3.1. How reliable is the pre-satellite period for atmospheric energetics?

First, we examine the climatological mean state of each component of the Lorenz energy cycle for the whole period (1958–2019) and the satellite period (1979–2019). From the viewpoint of the climatological mean state, no appreciable difference is found between the two time periods (not shown). However, there is a sudden jump before and after 1979 in the annual mean eddy available potential energy and eddy kinetic energy as shown in Fig. 1. We also find similar sudden jumps in the zonal mean available potential and kinetic energy reservoirs, while the differences of the zonal mean before and after 1979 are slightly smaller than those of the eddy energies. These sudden jumps were also reported by Marques et al. (2009) for other reanalysis datasets as a result of the introduction of satellite data in 1979. A non-parametric test – the Mann–Whitney U test (Nachar, 2008) – is used for examining the statistical difference between the two time periods. This test compares whether the distributions of the two samples of continuous observations belong to

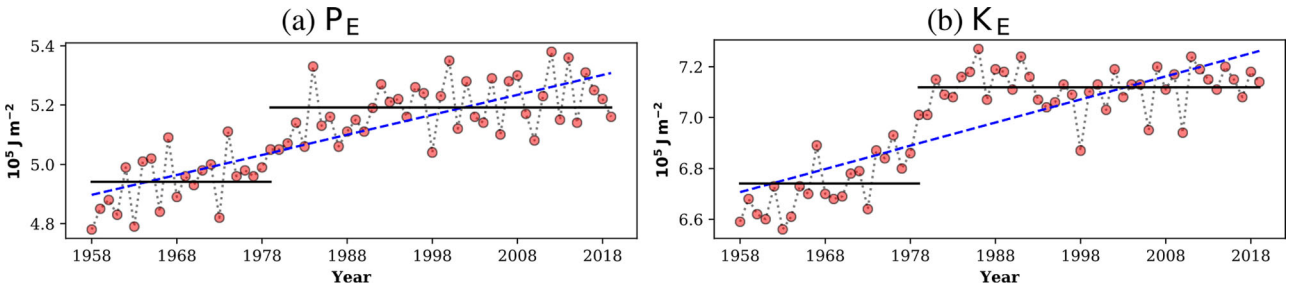

Fig. 1. Variations of eddy available potential energy (P_E) and eddy kinetic energy (K_E) for JRA-55 data. Solid black lines are averages over 1958–1979 and 1979–2019, respectively. Unit is $10^5 \mathrm{Jm}^{-2}$.

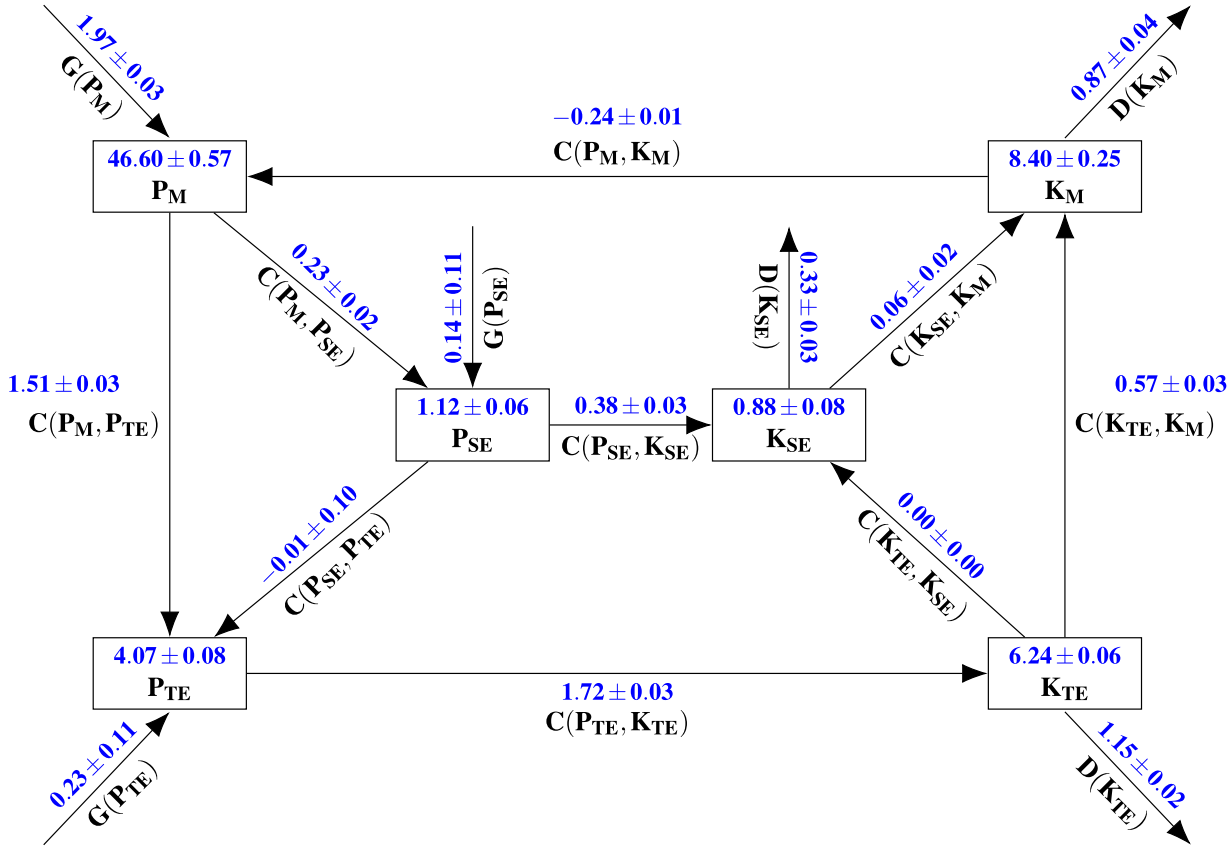

Fig. 2. The Lorenz energy cycle diagram from JRA-55 reanalysis dataset during 1979–2019. The uncertain range of the time-mean values stand for the standard deviations of the time series of the energy components. Units are $10^5 \mathrm{Jm}^{-2}$ for energy and Wm^{-2} for the conversion rate, generation, and dissipation terms. The arrows indicate the direction that corresponds to positive values. Negative values imply the opposite direction.

the same statistical population by determining if the medians are different or not (Ye and Ahammed, 2020). Results reveal that the differences are statistically significant at the 1% confidence level (two-tailed) among the zonal mean and eddy energies in the two time periods, except for P_M. This significant difference is also confirmed by using a two-sample *t*-test (Ye and Ahammed, 2020). Thus, we focus in the following on the Lorenz energy cycle during the satellite period 1979–2019.

3.2. Climatology of the Lorenz energy cycle

The climatological values of the global integrals of energies in the JRA-55 dataset are shown in Fig. 2. The order

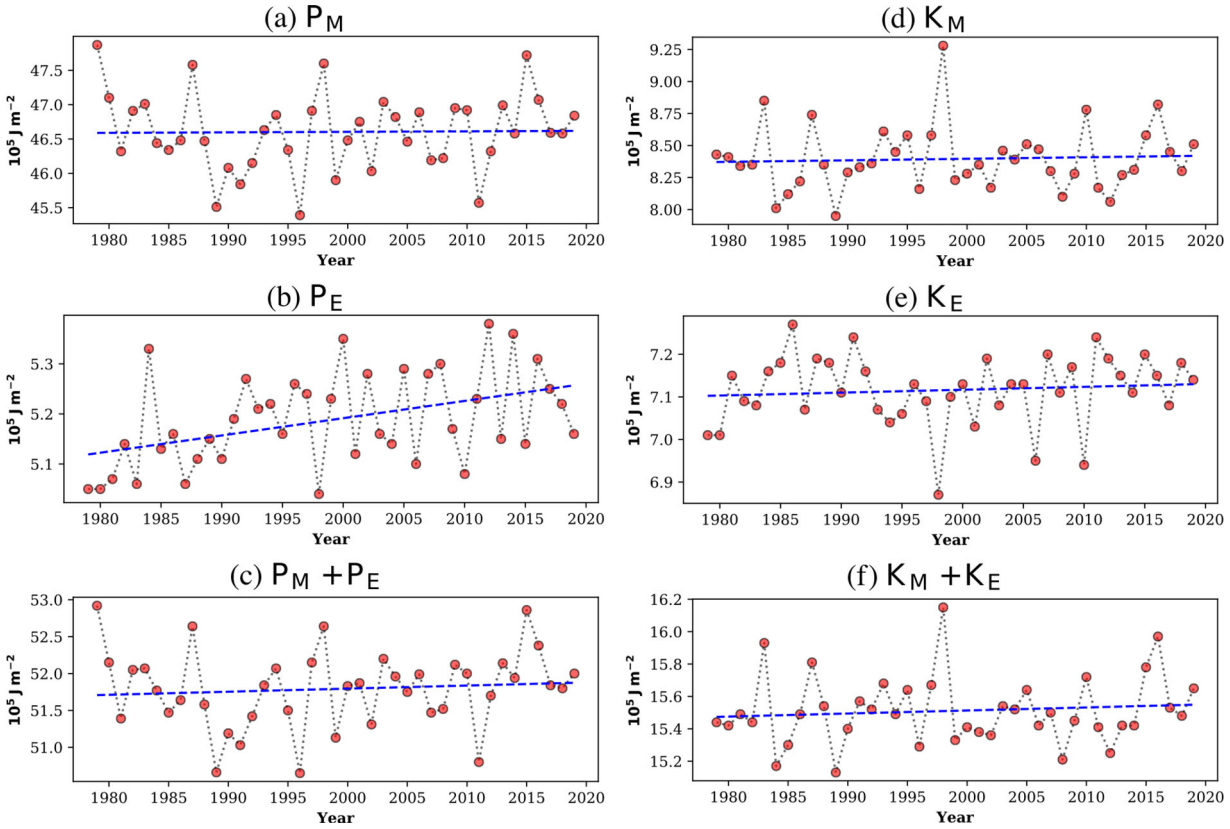

Fig. 3. Time series of the globally averaged atmospheric energies. (a) The mean available potential energy P_M. (b) The eddy available potential energy P_E. (c) The total available potential energy $P_M + P_E$. (d) The mean kinetic energy K_M. (e) The eddy kinetic energy K_E. (f) The total kinetic energy $K_M + K_E$.

of magnitude of the sum of the stationary P_{SE} and transient P_{TE} available potential energies is the same as the sum of the stationary K_{SE} and transient K_{TE} kinetic energies. The comparable order of magnitude between P_E and K_E is consistent with Li et al. (2007) and Lembo et al. (2019a). This is likely due to baroclinic instability which transforms available potential into kinetic energy instantaneously, mainly in mid-latitude weather systems, and which is driven by the meridional temperature gradient (Holton and Hakim, 2012). By trying to reduce this meridional temperature gradient, the atmosphere acts by reducing the available potential energy.

The time-mean values for all the energy components are comparable with other reanalysis datasets (Li et al., 2007; Marques et al., 2010; Pan et al., 2017), although the time-mean values of zonal mean energy components in our study are generally larger than those calculated from other reanalysis datasets. The discrepancies could be due to different vertical levels and time periods used for the integration of the energies. We also find that the time-mean values of the zonal mean energy components in our study are generally lower than the results from the climate models (Boer and Lambert, 2008; Lembo et al., 2019a). However, our results are in agreement with Marques et al. (2009).

3.3. Trends in global energies

Figure 3 displays the time series of the globally averaged mechanical energies P_M, P_E, K_M, and K_E between 1979 and 2019. All mechanical energies display an increasing linear trend, suggesting a general intensification of the global Lorenz energy cycle. We examine the significance of these linear trends with the Mann–Kendall test (Table 1). Among these energies, only P_E displays a significant upward trend of 390.48 Jm^{-2} per year.

The globally averaged conversion rates among the different mechanical energies are all increasing with time (Table 1). The linear trend is significant for $C(P_E, K_E)$ and $C(P_M, K_M)$ with a rate of 1.18 and 0.32 $10^{-3} Wm^{-2}$ per year, respectively. The increasing trend of $C(P_E, K_E)$ (Fig. 4) denotes a stronger mid-latitudinal baroclinic

instability induced by the sinking of colder air and rising warmer air (Kim and Kim, 2013). The significant positive correlation between $C(P_E, K_E)$ and temperature differences between the mid-latitudes and the polar regions for both hemispheres (see Sec. 3.7) suggests an increase in mid-latitudinal baroclinic instability. The trend of the $C(P_M, K_M)$ conversion rate links with the net effect of a number of processes occurring in the tropics and mid-latitudes, related to the activity of the Hadley ($C(P_M, K_M)>0$) and Ferrel cells ($C(P_M, K_M)<0$) (Li et al., 2007; Pan et al., 2017). As a significant trend exists, our results are consistent with an expansion of the Hadley cell over the past few decades (Seidel et al., 2008; Kang and Lu, 2012; Huang and McElroy, 2014; Davis and Davis, 2018).

The variations of $C(P_M, P_E)$ are associated with baroclinic disturbances, related to the meridional temperature gradient and Arctic amplification (Peixóto and Oort, 1974; Li et al., 2007). The temporal variations of large-scale weather systems in the mid-latitudes can also contribute to the trend of $C(P_M, P_E)$ (Pan et al., 2017). As, unlike in previous work (Pan et al., 2017), there is no clear trend for $C(P_M, P_E)$, we argue that these effects are somehow compensating. This result is consistent with Dai and Song (2020), who show that Arctic amplification in recent decades has little influence on northern mid-latitude weather. $C(K_E, K_M)$ is related to temporal variations of the jet streams in the troposphere (Kim and Kim, 2013). The slightly increasing trend of $C(K_E, K_M)$ thus suggests an increased poleward displacement of the jet streams as a result of the transport of momentum by the motion of eddies.

Table 1. Trends in the global energies.

	Global		
	Trend	Sig.	Unit
$\mathbf{P_M}$	344.09		$\mathbf{Jm^{-2}}$ per year
$\mathbf{P_E}$	390.48	**	$\mathbf{Jm^{-2}}$ per year
$\mathbf{P_M + P_E}$	543.75		$\mathbf{Jm^{-2}}$ per year
$\mathbf{K_M}$	188.06		$\mathbf{Jm^{-2}}$ per year
$\mathbf{K_E}$	121.06		$\mathbf{Jm^{-2}}$ per year
$\mathbf{K_M + K_E}$	214.42		$\mathbf{Jm^{-2}}$ per year
$\mathbf{C(P_M, P_E)}$	0.00		$\mathbf{10^{-3}Wm^{-2}}$ per year
$\mathbf{C(P_E, K_E)}$	1.08	*	$\mathbf{10^{-3}Wm^{-2}}$ per year
$\mathbf{C(K_E, K_M)}$	0.38		$\mathbf{10^{-3}Wm^{-2}}$ per year
$\mathbf{C(P_M, K_M)}$	–0.32	*	$\mathbf{10^{-3}Wm^{-2}}$ per year
$\mathbf{G(P_M)}$	0.53		$\mathbf{10^{-3}Wm^{-2}}$ per year
$\mathbf{G(P_E)}$	0.00		$\mathbf{10^{-3}Wm^{-2}}$ per year
$\mathbf{D(K_M)}$	1.45	*	$\mathbf{10^{-3}Wm^{-2}}$ per year
$\mathbf{D(K_E)}$	–0.44		$\mathbf{10^{-3}Wm^{-2}}$ per year

+at at 90% level.
*at 95% level.
**at 99% level.
***at 99.9% level.

Trends of the globally averaged generation and dissipation rates are examined and displayed in Table 1. All the generation and dissipation rates for the zonal mean mechanical energies ($G(P_M)$ and $D(K_M)$) are increasing with time. In particular, the positive linear trends in the dissipation rate of $D(K_M)$ are statistically significant at the 95% level (Fig. 5), which is mainly due to the increasing conversion rates related to transferring energies into K_M. Overall, the upward trend of the total dissipation rate of kinetic energies suggests an increasing efficiency of the global atmospheric thermal engine (Table 1), in agreement with (Pan et al., 2017).

3.4. Decomposition of global generation, dissipation, and conversion rates

Stationary and transient eddies both play important roles in the global energy cycle of the atmosphere (Ulbrich and Speth, 1991; Lembo et al., 2019a). Here, we decompose the eddy energies into stationary and transient components. Figure 2 shows that the magnitude of mechanical energy of transient eddies (P_{TE} and K_{TE}) is larger than that of stationary eddies (P_{SE} and K_{SE}); however, they have the same order of magnitude.

We first investigate the partition of the globally averaged generation rates. Although fluctuations exist (Figs. 6a and 6b), there are no statistically significant trends in $G(P_{SE})$ and $G(P_{TE})$. As for the decomposed globally

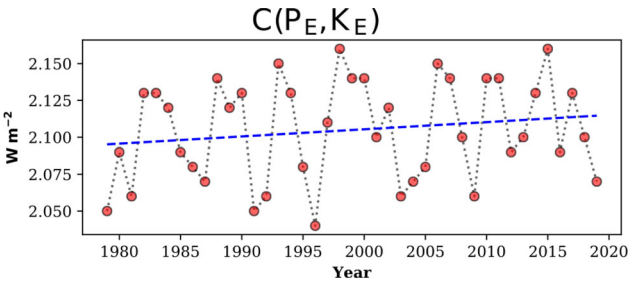

Fig. 4. Time series of the conversion rate between the eddy available potential energy and the eddy kinetic energy $C(P_E, K_E)$.

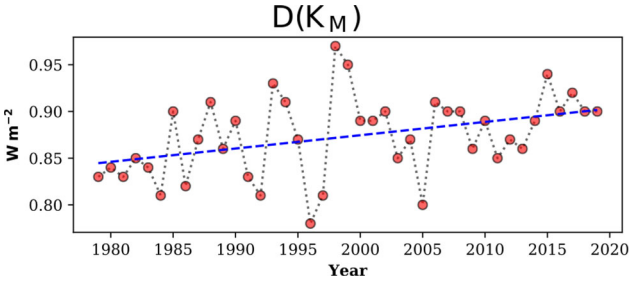

Fig. 5. The dissipation rate of the mean kinetic energy $D(K_M)$.

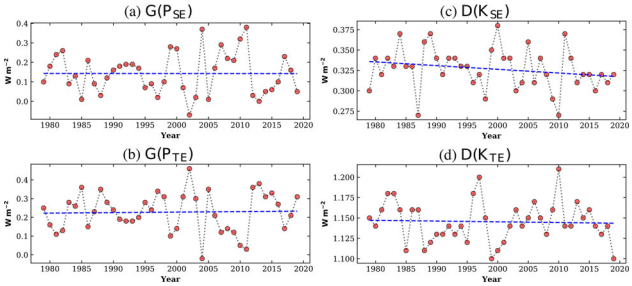

Fig. 6. Decomposed globally averaged generation and dissipation rates. (a) The generation rate of the stationary eddy available potential energy $G(P_{SE})$; (b) The generation rate of the transient eddy available potential energy $G(P_{TE})$; (c) The dissipation rate of the stationary eddy kinetic energy $D(K_{SE})$. (d) The dissipation rate of the transient eddy kinetic energy $D(K_{TE})$.

Table 2. Decomposition of global energies into eddies.

	Global		
	Trend	Sig.	Unit
$\mathbf{G(P_{SE})}$	–0.32		$10^{-3}\mathbf{Wm^{-2}}$ per year
$\mathbf{G(P_{TE})}$	0.48		$10^{-3}\mathbf{Wm^{-2}}$ per year
$\mathbf{D(K_{SE})}$	–0.45		$10^{-3}\mathbf{Wm^{-2}}$ per year
$\mathbf{D(K_{TE})}$	0.00		$10^{-3}\mathbf{Wm^{-2}}$ per year
$\mathbf{C(P_M, P_{SE})}$	0.00		$10^{-3}\mathbf{Wm^{-2}}$ per year
$\mathbf{C(P_M, P_{TE})}$	0.00		$10^{-3}\mathbf{Wm^{-2}}$ per year
$\mathbf{C(P_{SE}, P_{TE})}$	0.00		$10^{-3}\mathbf{Wm^{-2}}$ per year
$\mathbf{C(K_{TE}, K_M)}$	0.94	*	$10^{-3}\mathbf{Wm^{-2}}$ per year
$\mathbf{C(K_{SE}, K_M)}$	0.00		$10^{-3}\mathbf{Wm^{-2}}$ per year
$\mathbf{C(K_{TE}, K_{SE})}$	0.00		$10^{-3}\mathbf{Wm^{-2}}$ per year
$\mathbf{C(P_{TE}, K_{TE})}$	0.73	+	$10^{-3}\mathbf{Wm^{-2}}$ per year
$\mathbf{C(P_{SE}, K_{SE})}$	–0.35		$10^{-3}\mathbf{Wm^{-2}}$ per year

averaged dissipation rates (Figs. 6c and 6d), there is a significant negative linear trend in the time series of $D(K_{SE})$, but no significant trend in $D(K_{TE})$.

For the decomposed conversion rates of zonal and eddy available potential energies, as shown in Table 2, no significant trends are found for the conversion rates of $C(P_M, P_{SE})$ and $C(P_M, P_{TE})$, as well as $C(P_{SE}, P_{TE})$. However, in terms of the conversion rates between zonal and eddy kinetic energies, there is a significant upward linear trend in $C(K_{TE}, K_M)$, while $C(K_{SE}, K_M)$ and $C(K_{TE}, K_{SE})$ have no long-term trends (Table 2). The significant increasing trend of $C(K_{TE}, K_M)$ has a slope of $0.94 \times 10^{-3} Wm^{-2}$ per year (Fig. 7a). The trends of $C(K_{TE}, K_M)$ are likely linked to the increasing trend of $C(K_E, K_M)$ in Table 1. This indicates the strengthening of horizontal transport of momentum and energy from eddies to the zonal mean flow (K_M).

In addition to that, as denoted in Table 1, the conversion rate of $C(P_E, K_E)$ presents a significantly increasing trend. Here, we mainly attribute this increasing trend to the significant trend of $C(P_{TE}, K_{TE})$ (Fig. 7b and Table 2), as $C(P_{SE}, K_{SE})$ displays insignificantly negative trend. Our results suggest that baroclinic instability is becoming stronger, leading to more unstable weather systems mainly in the mid-latitudes through transient eddies.

3.5. Hemispheric differences in eddy potential and kinetic energies

We consider the averaged eddy available potential and kinetic energies separately in the Northern and Southern hemispheres (Fig. 8). As shown in Figs. 8a and 8b, all the components of P_E are larger in the Northern Hemisphere than in the Southern Hemisphere. Concerning the trends, components of P_E experience an increasing trend, except for P_{SE} in the Southern Hemisphere (Table 3). Our results suggest that the globally increasing trend of P_E (Table 1) is mainly due to the significantly increasing trend in P_{TE} in the Southern Hemisphere. The conversion

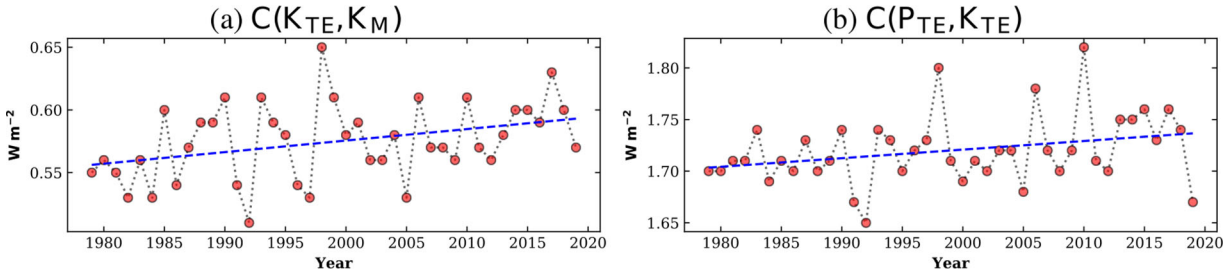

Fig. 7. Decomposed globally averaged conversion rates. (a) The conversion rate between the transient eddy kinetic energy and mean kinetic energy $C(K_{TE}, K_M)$; (b) The conversion rate between the transient eddy kinetic energy and transient eddy kinetic energy $C(P_{TE}, K_{TE})$.

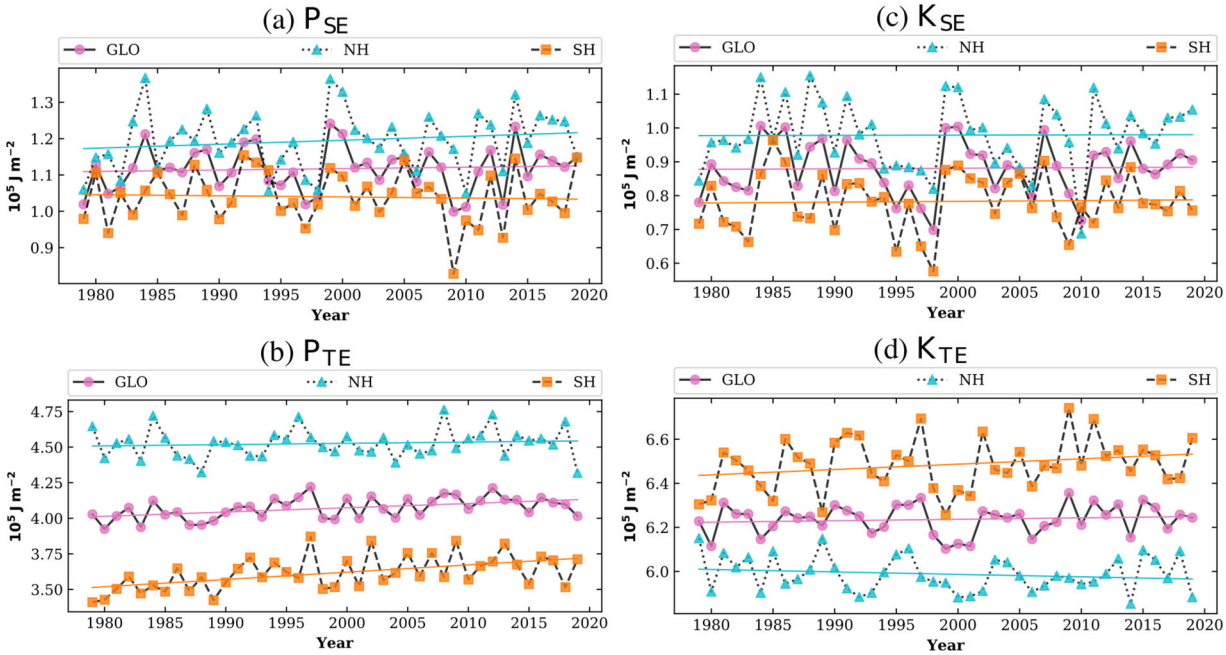

Fig. 8. Decomposed the globally averaged eddy available potential energy and kinetic energy. (a) The stationary eddy available potential energy P_{SE}; (b) The transient eddy available potential energy P_{TE}; (c) The stationary eddy kinetic energy K_{TE}; (d) The transient eddy kinetic energy K_{TE}.

Table 3. Decomposition of potential and kinetic energy ($\mathbf{Jm^{-2}}$ per year).

		Global		NH		SH	
		Trend	Sig.	Trend	Sig.	Trend	Sig.
$\mathbf{P_E}$	$\mathbf{P_{TE}}$	315.14	**	132.24		539.17	***
	$\mathbf{P_{SE}}$	61.90		100.00		–20.00	
$\mathbf{K_E}$	$\mathbf{K_{TE}}$	54.77		–106.11		242.58	
	$\mathbf{K_{SE}}$	–1.35		83.33		37.72	

of available potential energy from the zonal mean to transients involves the meridional transport of heat (Ulbrich and Speth, 1991). In this respect, our results suggest an increase of the meridional temperature perturbation at the troposphere in the Southern Hemisphere, which is in agreement with Pan et al. (2017). Indeed, we find that the vertically averaged meridional temperature gradient in the troposphere over the Southern Hemisphere ΔT_{SH} has a statistically significant increasing trend (not shown).

As for trends of the components decomposed from the eddy kinetic energy, the results of the linear trends shown in Fig. 8c and 8d are well in agreement with Table 3. An upward trend is found in K_{TE} mainly over the Southern Hemisphere, responsible for the overall increasing trend of K_E (Table 1). K_{SE} has a slightly negative trend at the global scale, however, it has positive trends in both hemispheres. The strong interannual variations in K_{SE} on the hemispheric scale could explain the slightly negative trend on the global scale, as the global K_{SE} is calculated by

Table 4. The climatological eddy available potential and kinetic energy on different wave-number domain during 1979–2019 ($\mathbf{Jm^{-2}}$ per year).

	Group	GLO	NH	SH		Group	GLO	NH	SH
$\mathbf{P_{SE}}$	PW	0.66	0.63	0.69	$\mathbf{K_{SE}}$	PW	0.47	0.46	0.49
	SW	0.25	0.24	0.25		SW	0.23	0.28	0.18
	MW	0.02	0.02	0.02		MW	0.02	0.02	0.02
	SUM	0.92	0.89	0.96		SUM	0.71	0.75	0.68
	Percent	82.57%	74.11%	92.24%		Percent	81.11%	76.40%	86.93%
$\mathbf{P_{TE}}$	PW	1.04	1.28	0.80	$\mathbf{K_{TE}}$	PW	0.92	1.02	0.82
	SW	1.86	1.87	1.84		SW	3.38	2.98	3.79
	MW	0.26	0.29	0.24		MW	0.72	0.75	0.69
	SUM	3.16	3.44	2.88		SUM	5.02	4.75	5.29
	Percent	77.59%	75.96%	79.63%		Percent	80.50%	79.26%	81.64%

averaging the K_{SE} from the two hemispheric scales. These results indicate that the storm tracks altogether may be intensifying along with poleward shifts of the jet streams (Li et al., 2007), especially in the Southern Hemisphere.

3.6. Wave number decomposition of the global eddy energies

3.6.1. The climatological mean state. As expected, planetary-scale waves dominate P_{SE} on global and hemispheric scales. The sum of the energies in the three-wave number groups represents around 83% of P_{SE} over the globe, 74% in the Northern Hemisphere, and 92% in the Southern Hemisphere (Table 4 and Fig. 2). As for P_{TE}, the contribution of planetary-scale waves is comparable, though slightly smaller than the one from synoptic-scale waves at the global and the Northern Hemispheric scales, and more than 2 times smaller over the Southern Hemisphere. In general, the energy of meso-scale waves only makes a modest contribution.

Similar to those related to P_E, the energy of planetary-scale waves also dominates K_{SE} on a global and a hemispheric scale, followed by synoptic-scale waves and meso-scale waves. The percentage of the sum of the three wave-number groups of K_{SE} accounts for around 81% of K_{SE} at a global scale. As expected, the synoptic-scale waves generally make the most substantial contributions in K_{TE}, which is $3-4$ times bigger than planetary-scale waves and meso-scale waves at the global and Southern Hemispheric scales.

Overall, the percentage of the sum of the three wave-number groups for the transient eddy energies is smaller than those for stationary eddy energy, except for the energies over the Northern Hemisphere. This indicates that besides the meso-scale waves, small-scale waves (wave-numbers larger than 21) are also playing an important role in carrying and transforming transient eddy energies, especially over the Northern Hemisphere.

3.6.2. Trends of eddy energies. We focus now on the trends of the wave-number groups (Fig. 9 and Table 5). For P_{SE}, the energies embedded in planetary-scale waves show a negative trend in the Southern Hemisphere (Fig. 9a), and the negative trend exists in the energies associated with the synoptic-scale waves in the Northern Hemisphere as well. These decreased trends lead to a negative trend of P_{SE} for the sum of energies of those three wave-number groups (Table 5). In contrast, an insignificant positive trend of P_{SE} is identified (Table 3). This contradictory result can be inferred from the contributions from small-scale waves in P_{SE}.

In terms of P_{TE}, the energy carried by synoptic-scale waves exhibits a clear positive trend (Fig. 9b and Table 5). These positive trends are all significant at the 95% level, especially for the Southern Hemispheric and global scales with the significance level at 99.9%. The energies of meso-scale waves exhibit a significant increasing trend as well, except in the Northern Hemisphere. These significant positive trends suggest an increase in baroclinic disturbances in the mid- and high-latitudes over both hemispheres, in agreement with Hu et al. (2004). Furthermore, the increasing trends in the energies of the three wave number groups explain the positive trend of P_{TE} (Table 5).

Although all the components related to K_E present insignificant trends in Table 3, the decomposition of those components into different wave-number groups provide valuable information. The negative trend of K_{SE} can likely be attributed to the global decline in the energies within all three wave-number groups (Table 5), especially the significant negative trend of energies with meso-scale waves. Although energies within planetary-scale waves are dominant in the climatological K_{SE}, the trends of this energy component are not statistically significant (Fig. 9c). As for the globally increasing trend of K_{TE} in Table 3, it stems mainly from the significant upward trend of energies provided by synoptic-scale waves,

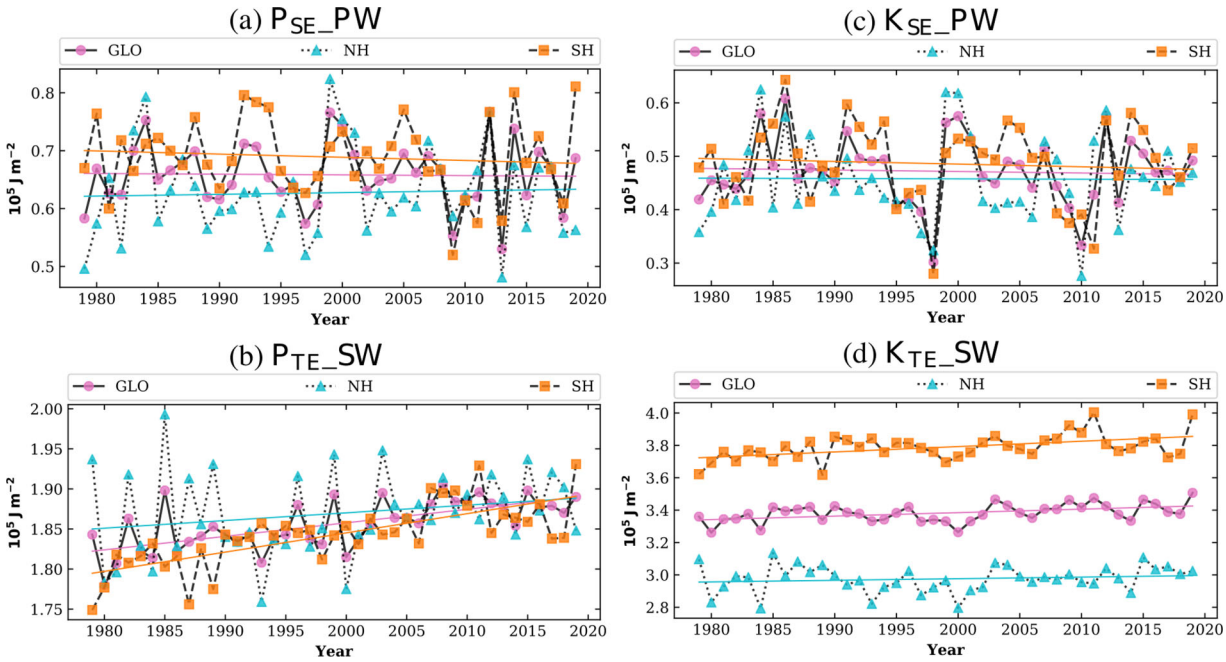

Fig. 9. Decomposed the stationary and transient eddy energies into wave-number domain. (a) Energies in Planetary-scale Waves group for the stationary eddy available potential energy $P_{SEP}W$; (b) Energies in Synoptic-scale Waves group for the transient eddy available potential energy $P_{TES}W$; (c) Energies in Planetary-scale Waves group for the stationary eddy kinetic energy $K_{SEP}W$; (d) Energies in Synoptic-scale Waves group for the transient eddy kinetic energy $K_{TES}W$.

Table 5. Decomposition of mechanical energy into wave number domain (**Jm^{-2}** per year).

		Global		NH		SH	
		Trend	Sig.	Trend	Sig.	Trend	Sig.
P_{SE}	PW	–3.57		57.19		–51.92	
	SW	–23.75		–44.10	+	8.01	
	MW	–0.00	*	0.00		–5.00	***
	SUM	–32.29		–55.14		–53.49	
P_{TE}	PW	88.23		10.43		177.37	+
	SW	176.47	***	146.86	*	225.66	***
	MW	12.50	*	1.35		16.67	*
	SUM	279.40	***	78.24		448.81	***
K_{SE}	PW	–6.93		24.17		–40.00	
	SW	–0.00		–50.81		33.81	
	MW	–2.94	***	0.00	+	–3.28	**
	SUM	–50.55		–67.42		–14.64	
K_{TE}	PW	–100.00	+	–120.61		–62.35	
	SW	210.17	**	93.52		276.03	**
	MW	–0.00		–29.86		26.79	
	SUM	103.85		–34.72		252.66	+

especially over the Southern Hemisphere (Fig. 9d), although the trend for K_{TE} within planetary-scale waves is significantly negative at the global scale. Our results implicitly suggest a poleward shift of the tropospheric jets and intensifying storm tracks, mainly occurring over the Southern Hemisphere (Li et al., 2007; Kim and Kim, 2013).

3.7. The impact of modes of climate variability on the Lorenz energy cycle

3.7.1. Analysis of the correlations. We calculate the Pearson correlation between detrended Lorenz energy cycle components and climate indices as mentioned in section 2 (Tables 6 and 7). The significance of the correlation is tested based on the two-tailed student's *t*-test. As shown in Table 6, P_M presents a close relationship with most climate indices, except NAO, QBO, AMO, and ΔT_{NH}. The total available potential energy ($P_M + P_E$) is dominated by P_M and therefore shares nearly the same correlation with P_M. As for P_E, it seems unrelated to most of the indices, except for AMO, GMST, and ΔT_{SH}, and it tends to have correlations of the opposite sign compared with P_M. The significant correlation with ΔT_{SH} is consistent with Li et al. (2007), where they found that variation of P_E is associated with the land-sea temperature contrast mainly over the Southern Hemisphere. By decomposing P_E (Table 7), we find that P_{SE} and P_{TE} contribute differently to the variations of P_E in different hemispheres. P_{SE} has stronger correlations with atmospheric indices over the Northern Hemisphere, while P_{SE}

Table 6. Correlations between climate indices and different global Lorenz energy cycle components.

	$P_M + P_E$	$K_M + K_E$	P_M	P_E	K_M	K_E	$C(P_M, P_E)$
AO	–0.31*	–0.21	–0.32*	0.16	–0.29+	0.35*	0.01
NAO	–0.19	–0.19	–0.21	0.22	–0.31+	0.46**	–0.07
*NINO*3.4	0.54***	0.47**	0.53***	–0.20	0.41**	–0.04	0.05
PNA	0.30+	0.61***	0.30+	–0.17	0.56***	–0.15	0.26+
SAM	0.26+	0.24	0.27+	–0.19	0.33*	–0.38*	0.31*
QBO	–0.08	0.09	–0.04	–0.23	0.06	0.07	0.17
PDO	0.44**	0.56***	0.43**	–0.10	0.47**	–0.03	0.26+
AMO	0.20	0.29*	0.23	–0.28+	0.38*	–0.43**	0.13
GMST	0.47**	0.68***	0.52***	–0.49**	0.69***	–0.39*	0.18
ΔT_{NH}	–0.07	–0.01	–0.07	0.01	–0.04	0.09	0.18
ΔT_{SH}	0.32*	0.21	0.36*	–0.39*	0.35*	–0.52***	0.46**
	$C(P_E, K_E)$	$C(K_E, K_M)$	$C(P_M, K_M)$	G_{PM}	G_{PE}	D_{KM}	D_{KE}
AO	0.35*	0.19	0.00	0.01	0.49**	0.17	0.21
NAO	0.13	0.04	0.02	–0.08	0.27+	0.03	0.12
*NINO*3.4	–0.17	–0.13	0.02	0.04	–0.30+	–0.12	–0.05
PNA	0.07	0.08	0.09	0.20	–0.16	0.05	–0.02
SAM	0.35*	0.41**	–0.22	0.38*	0.19	0.41**	–0.09
QBO	0.09	0.26+	–0.09	0.19	–0.04	0.25	–0.24
PDO	–0.08	–0.05	0.13	0.18	–0.37*	–0.08	–0.03
AMO	0.05	0.13	0.00	0.12	–0.06	0.11	–0.10
GMST	0.07	0.21	–0.10	0.21	–0.08	0.21	–0.20
ΔT_{NH}	0.39*	0.26	0.10	0.12	0.38*	0.20	0.17
ΔT_{SH}	0.4*	0.46**	–0.03	0.43**	0.11	0.41**	–0.10

Table 7. Correlations between climate indices and different eddies Lorenz energy cycle components at different scales.

	Global				NH				SH			
	P_{SE}	P_{TE}	K_{SE}	K_{TE}	P_{SE}	P_{TE}	K_{SE}	K_{TE}	P_{SE}	P_{TE}	K_{SE}	K_{TE}
AO	0.20	0.03	0.27+	0.13	0.23	–0.00	0.40**	0.10	0.08	0.04	0.02	0.08
NAO	0.31*	0.00	0.42**	0.09	0.40**	0.01	0.47**	0.20	0.08	–0.01	0.22	–0.03
NINO3.4	–0.29+	–0.00	–0.36*	0.39*	–0.33*	–0.22	–0.33*	–0.00	–0.12	0.22	–0.27+	0.46**
PNA	0.09	–0.31*	–0.12	–0.04	0.08	–0.41**	–0.05	–0.20	0.06	0.01	–0.17	0.10
SAM	–0.11	–0.15	–0.26+	–0.18	–0.09	0.23	–0.28+	0.28+	–0.09	–0.43**	–0.16	–0.40**
QBO	–0.07	–0.21	–0.05	0.16	–0.07	–0.44**	0.07	–0.04	–0.04	0.17	–0.17	0.21
PDO	0.06	–0.19	–0.17	0.18	0.01	–0.25	–0.17	0.08	0.08	0.01	–0.12	0.15
AMO	–0.17	–0.21	–0.35*	–0.12	–0.17	–0.11	–0.33*	0.04	–0.10	–0.16	–0.27+	–0.17
GMST	–0.33*	–0.34*	–0.50***	0.12	–0.32*	–0.35*	–0.39*	0.09	–0.21	–0.09	–0.46**	0.08
ΔT_{NH}	0.00	0.01	0.01	0.12	0.00	–0.05	0.16	0.01	0.00	0.07	–0.16	0.13
ΔT_{SH}	–0.20	–0.33*	–0.32*	–0.28+	–0.10	0.18	–0.36*	0.18	–0.23	–0.60***	–0.17	–0.45**

is responsible for the significant negative correlation between P_E and ΔT_{SH} occurring over the Southern Hemisphere. This is suggestive of the peculiar role of orographically forced stationary Rossby waves in the Southern Hemisphere, adding details on the importance of the land-sea contrast described in Li et al. (2007).

K_M experiences a strong relationship with all climate indices, except QBO and ΔT_{NH}. The total kinetic energy ($K_M + K_E$) shares the same correlations as K_M (Table 6). As for K_E, it is affected mainly by atmospheric and temperature indices and tends to represent the opposite correlations compared with K_M for most indices. Our results show that the modes of climate variability more strongly affect the eddy kinetic energy than the available potential energy, in particular, the impacts of long-lived oceanic variability (PDO and AMO). As shown in Table 7, we find that correlations for K_E with climate indices in Table 6 are dominated by K_{SE}, especially over the Northern Hemisphere.

Concerning the correlations in conversion rates (Table 6), $C(P_M, P_E)$ has a significant positive correlation with PNA, SAM, PDO, and ΔT_{SH}. As $C(P_M, P_E)$ is

related to mid-latitude cyclones and anticyclones (Li et al., 2007), these correlations indicate that its variations link with the fluctuations in the jet stream over the PNA and associate with the meridional heat transport mainly over the Southern Hemisphere. $C(P_E, K_E)$ has significant correlations with the AO, SAM, ΔT_{NH}, and ΔT_{SH}, which suggests that its variations are connected with heat-driven rising and sinking motions through strengthening temperature perturbations in the troposphere over mid-latitudes (Li et al., 2007; Pan et al., 2017). $C(K_E, K_M)$ is associated with the changes in the positions of the jet streams in the troposphere (Li et al., 2007), and it has a significant positive correlation with the QBO, SAM, and ΔT_{SH}. Our results illustrate that the variations of $C(K_E, K_M)$ occur mainly over the Southern Hemisphere and are affected by the zonal wind variations in the tropical lower stratosphere. As for $C(P_M, K_M)$, it presents no significant correlation with climate indices. Our results suggest that the selected climate indices do not play a role in converting changes in the energy conversions mediated by the zonal mean flow and changes in the strength of the zonal mean mass-circulation itself at the global scale. However, we should be cautious in interpreting these correlation results as a cause-effect relationship. What our results show is that the respective climate variability modes develop in line with the conversions rates they correlate with. The cause-effect relationships cannot be inferred with correlations.

3.7.2. The mechanisms behind the correlations. Results from the correlations illustrate that the indices of NINO3.4, AO, and SAM contribute the most to the variation of the Lorenz energy cycle. In terms of the zonal mean energetics, the NAO, PDO, and AMO play an important role as well, especially for the zonal mean kinetic energy. ENSO has indeed a well-known strong impact on global mean temperatures, so it is not surprising that ENSO affects the Lorenz energy cycle, particularly during El Niño and La Niña years (Li et al., 2011; Trenberth and Fasullo, 2013). ENSO causes enhanced tropical heating as well, which in turn excites both quasi-stationary and poleward propagating Rossby waves (Sardeshmukh and Hoskins, 1988; Franzke et al., 2011; Feldstein and Franzke, 2017). We speculate that these Rossby waves, triggering NAO events (Cassou, 2008; Franzke et al., 2019), explain the role of the NAO in the variation of eddy energies. The PNA also has strong impacts on the zonal mean flow (e.g. Feldstein and Franzke, 2017) and, thus, affects zonal mean energetics (Castanheira and Marques, 2019; Martineau et al., 2020).

As mentioned, the PDO contributes to the variations of zonal mean energetics, while the AMO is more important for eddy kinetic energies. Being the most dominant SST variability mode in the Pacific Ocean on low-frequency timescales (Sohn et al., 2013), the PDO can modulate the interannual variations of ENSO and is associated with the Walker Circulation (Seidel et al., 2008), thus having an impact on the variations of the Lorenz energy cycle consistent with Veiga et al. (2013). On the contrary, variations of the AMO are connected with the meridional sea surface temperature anomalies, which likely influence the atmospheric circulation (Frajka-Williams et al., 2017) and therefore are associated with the variations of P_E and as a consequence, possibly with K_E and K_M.

The meridional temperature gradients are driving the meridional circulations and their related energy transformations (Makarieva et al., 2017). As sharp topographic and thermal contrasts exist, the Antarctic and subantarctic regions are characterised by the very energetic nature of synoptic activity (Simmonds et al., 2003). Thus, it is not surprising that the variations of the Lorenz energy cycle tend to have significant correlations with ΔT_{SH} over the Southern Hemisphere for most of the Lorenz energy cycle components, especially for the eddy available potential and kinetic energies.

4. Conclusion

Here we investigate the atmospheric Lorenz energy cycle and its spatio-temporal variability using the JRA-55 reanalysis. We first calculate the Lorenz energy cycle from 1958 to 2019 and find that a clear sudden jump exists in the zonal mean and eddy energies around 1979, likely due to the introduction of satellite data in that year, introducing an inhomogeneity into components of the Lorenz energy cycle. Thus, we decided to focus on the trends and variability of the Lorenz energy cycle between 1979 and 2019. Our main results can be summarised as follows:

- The total mechanic energy in the troposphere did not significantly change during the period 1979–2019. However, the eddy available potential energy exhibits significant positive trends, especially the transient eddy available potential energy in the Southern Hemisphere. This is consistent with an increase in storm track strength in the Southern Hemisphere (Franzke and Harnik, submitted).
- The conversion rates between eddy available potential and eddy kinetic energy, and between zonal mean available potential and zonal mean kinetic energy have significantly increased. The significant trend of the former is mainly through transient eddies, and indicates the strengthening of baroclinic eddy activity in the climate system; the latter suggests

a role played in the expansion of the Hadley cell over the last few recent decades.

- A decomposition of the eddy energies into different wave-number groups shows that the energies of planetary-scale waves dominate the stationary eddy energies; the energy carried by synoptic-scale waves dominates the transient eddy energies with a significant increasing trend. Results confirm recent findings on the intensification of eddy activity (Pan et al., 2017) and synoptic-scale waves (Chemke and Ming, 2020).
- Correlations between the Lorenz energy cycle and climate indices reveal the tight relation between the temporal variations of most Lorenz energy cycle components and atmospheric and oceanic indices. Among those indices, NINO3.4, AO, SAM, and PDO contribute most to the interannual variability of the Lorenz energy cycle. The correlations with vertical averaged temperature differences indicate that the variations of Lorenz energy cycle are more related to the meridional heat transport over the Southern Hemisphere. While most correlations with modes of climate variability have modest correlation values, these modes nevertheless have a significant impact on the Lorenz energy cycle.

The physical relevance of trends depends closely on the length of the time series. Here we were able to use the period 1979–2019. The pre-satellite period 1958–1978 was not usable because of a significant jump in between these two periods. This calls for an improvement of satellite data assimilation in reanalysis data sets. Results suggest that eddy energetics are underestimated, before the satellite revolution, but to clarify this, further research is needed.

The Lorenz energetics are integrated from a quasi-hydrostatic dry atmosphere. Since anthropogenic global warming will potentially lead to more water vapour in the atmosphere, it would be beneficial to also include the effects of moisture and latent heat in the energy cycle. Current attempts focus mainly on the moist static energy (Neelin and Held, 1987; Barpanda and Shaw, 2017; Shaw et al., 2018). These studies also focus either on the tropics or on mid-latitude storm tracks. A global picture of how increasing moisture in the atmosphere will affect the energetics and the circulation is still missing and hinders the attempt to better understand and predict the effects of global warming.

The results presented in this paper show that the variations of the energetics can be used to help to evaluate atmospheric general circulation models and to diagnose the intensification of the eddy activity in the climate system. As part of our future research, results will be used to systematically evaluate and constrain the latest generation of Earth System Models of the Coupled Model Intercomparison Project phase 6 (CMIP6). The scope of our current research is limited to the global and hemispheric annual time-series as well. Future research on the temporal and spatial variation of energetics at a shorter- and finer-scale will further improve our understanding of the climate system.

Acknowledgements

We thank the anonymous reviewers and the editor for their constructive comments.

Disclosure statement

No potential conflict of interest was reported by the authors.

Funding

This study was partly supported by the collaborative research center TRR181 “Energy transfers in atmosphere and ocean” funded by the German Research Foundation. QM was financially supported by the Chinese Scholarship Council.

References

Ambaum, M. H. 2010. *Thermal Physics of the Atmosphere*. Chichester, UK: John Wiley & Sons Ltd.

Barpanda, P. and Shaw, T. 2017. Using the moist static energy budget to understand storm-track shifts across a range of time scales. *J. Atmos. Sci.* **74**, 2427–2446. doi:10.1175/JAS-D-17-0022.1

Boer, G. J. and Lambert, S. 2008. The energy cycle in atmospheric models. *Clim. Dyn.* **30**, 371–390. doi:10.1007/s00382-007-0303-4

Cassou, C. 2008. Intraseasonal interaction between the Madden-Julian Oscillation and the North Atlantic oscillation. *Nature* **455**, 523–527. doi:10.1038/nature07286

Castanheira, J. M. and Marques, C. A. 2019. The energy cascade associated with daily variability of the north atlantic oscillation. *Q. J. R. Meteorol. Soc.* **145**, 197–210. doi:10.1002/qj.3422

Chemke, R. and Ming, Y. 2020. 2020: Large atmospheric waves will get stronger while small waves will get weaker by the end of the 21st century. *Geophys. Res. Lett.* **47**, e2020GL090441.

Clément, M., Nikiéma, O. and Laprise, R. 2017. Limited-area atmospheric energetics: illustration on a simulation of the crcm5 over eastern north America for december 2004. *Clim. Dyn.* **48**, 2797–2818. doi:10.1007/s00382-016-3198-0

Dai, A. and Song, M. 2020. Little influence of arctic amplification on mid-latitude climate. *Nat. Clim. Chang.* **10**, 231–237. doi:10.1038/s41558-020-0694-3

Davis, N. and Davis, S. M. 2018. Reconciling hadley cell expansion trend estimates in reanalyses. *Geophys. Res. Lett.* **45**, 11–439.

Feldstein, S. B. and Franzke, C. L. E. 2017. Atmospheric teleconnection patterns. In: *Nonlinear and Stochastic Climate Dynamics* (eds. L. E. Franzke, and T. O'Kane). Cambridge, UK: Cambridge University Press, pp. 54–104.

Frajka-Williams, E., Beaulieu, C. and Duchez, A. 2017. Emerging negative atlantic multidecadal oscillation index in spite of warm subtropics. *Sci. Rep.* **7**, 1–8.

Franzke, C. L. E., Feldstein, S. B. and Lee, S. 2011. Synoptic analysis of the Pacific–North American teleconnection pattern. *Q. J. R. Meteorol. Soc.* **137**, 329–346. doi:10.1002/qj.768

Franzke, C. L. E., Jelic, D., Lee, S. and Feldstein, S. B. 2019. Systematic decomposition of the MJO and its Northern Hemispheric extratropical response into Rossby and inertio-gravity components. *Q. J. R. Meteorol. Soc.* **145**, 1147–1164. doi:10.1002/qj.3484

Franzke, C. L. E. and Torelló I Sentelles, H. 2020. Mortality risks and modes of climate variability. *Clim. Change* **162**, 141–157.

Gocic, M. and Trajkovic, S. 2013. Analysis of changes in meteorological variables using mann-kendall and sen's slope estimator statistical tests in serbia. *Global Planet. Change* **100**, 172–182. doi:10.1016/j.gloplacha.2012.10.014

Hannachi, A., Straus, D. M., Franzke, C. L. E., Corti, S. and Woollings, T. 2017. Low-frequency nonlinearity and regime behavior in the Northern Hemisphere extratropical atmosphere. *Rev. Geophys.* **55**, 199–234. URL, 2015RG000509. doi:10.1002/2015RG000509

Hernández-Deckers, D. and von Storch, J.-S. 2010. Energetics responses to increases in greenhouse gas concentration. *J. Clim.* **23**, 3874–3887. doi:10.1175/2010JCLI3176.1

Holton, J. R. and Hakim, G. J. 2012. *An Introduction to Dynamic Meteorology*, Vol. 88. Burlington, MA: Academic Press.

Hu, Q., Tawaye, Y. and Feng, S. 2004. Variations of the northern hemisphere atmospheric energetics: 1948–2000. *J. Climate* **17**, 1975–1986. doi:10.1175/1520-0442(2004)017<1975:VOTNHA>2.0.CO;2

Huang, J. and McElroy, M. B. 2014. Contributions of the hadley and ferrel circulations to the energetics of the atmosphere over the past 32 years. *J. Clim.* **27**, 2656–2666. doi:10.1175/JCLI-D-13-00538.1

Kang, S. M. and Lu, J. 2012. Expansion of the hadley cell under global warming: Winter versus summer. *J. Clim.* **25**, 8387–8393. doi:10.1175/JCLI-D-12-00323.1

Kim, Y.-H. and Kim, M.-K. 2013. Examination of the global Lorenz energy cycle using merra and ncep-reanalysis 2. *Clim. Dyn.* **40**, 1499–1513. doi:10.1007/s00382-012-1358-4

Kobayashi, S., Ota, Y., Harada, Y., Ebita, A., Moriya, M., and co-authors. 2015. The jra-55 reanalysis: General specifications and basic characteristics. *J. Meteorol. Soc. Japan* **93**, 5–48. doi:10.2151/jmsj.2015-001

Lembo, V., Lunkeit, F. and Lucarini, V. 2019a. Thediato (v1.0)–a new diagnostic tool for water, energy and entropy budgets in climate models. *Geosci. Model Dev.* **12**, 3805–3834. doi:10.5194/gmd-12-3805-2019

Lembo, V., Messori, G., Graversen, R. and Lucarini, V. 2019b. Spectral decomposition and extremes of atmospheric meridional energy transport in the northern hemisphere midlatitudes. *Geophys. Res. Lett.* **46**, 7602–7613. doi:10.1029/2019GL082105

Li, L., Ingersoll, A. P., Jiang, X., Feldman, D. and Yung, Y. L. 2007. Lorenz energy cycle of the global atmosphere based on reanalysis datasets. *Geophys. Res. Lett.* **34**, L16813.

Li, L., Jiang, X., Chahine, M. T., Wang, J. and Yung, Y. L. 2011. The mechanical energies of the global atmosphere in el niño and la niña years. *J. Atmos. Sci.* **68**, 3072–3078. doi:10.1175/JAS-D-11-072.1

Lorenz, E. N. 1955. Available potential energy and the maintenance of the general circulation. *Tellus* **7**, 157–167.

Lucarini, V., Fraedrich, K. and Ragone, F. 2011. New results on the thermodynamic properties of the climate system. *J. Atmos. Sci.* **68**, 2438–2458. URL https://journals.ametsoc.org/jas/article/68/10/2438/27096/New-Results-on-the-Thermodynamic-Properties-of-the. doi:10.1175/2011JAS3713.1

Makarieva, A., Gorshkov, V., Nefiodov, A., Sheil, D., Nobre, A. and co-authors. 2017. Kinetic energy generation in heat engines and heat pumps: the relationship between surface pressure, temperature and circulation cell size. *Tellus A: Dyn. Meteorol. Oceanograph.* **69**, 1272752. doi:10.1080/16000870.2016.1272752

Mann, H. B. 1945. Nonparametric tests against trend. *Econometrica* **13**, 245–259. doi:10.2307/1907187

Marques, C., Rocha, A. and Corte-Real, J. 2010. Comparative energetics of era-40, jra-25 and ncep-r2 reanalysis, in the wave number domain. *Dyn. Atmos. Oceans* **50**, 375–399. doi:10.1016/j.dynatmoce.2010.03.003

Marques, C. A., Rocha, A., Corte-Real, J., Castanheira, J. M., Ferreira, J. and co-authors. 2009. Global atmospheric energetics from ncep–reanalysis 2 and ecmwf–era40 reanalysis. *Int. J. Climatol.* **29**, 159–174. doi:10.1002/joc.1704

Martineau, P., Nakamura, H., Kosaka, Y. and Yamamoto, A. 2020. Importance of a vertically tilting structure for energizing the north atlantic oscillation. *Sci. Rep.* **10**, 1–10.

Nachar, N. 2008. The Mann-Whitney U: a test for assessing whether two independent samples come from the same distribution. *Tutor Quant. Methods Psychol.* **4**, 13–20. doi:10.20982/tqmp.04.1.p013

Neelin, J. D. and Held, I. M. 1987. Modeling tropical convergence based on the moist static energy budget. *Mon. Wea. Rev.* **115**, 3–12. doi:10.1175/1520-0493(1987)115<0003:MTCBOT>2.0.CO;2

Pan, Y., Li, L., Jiang, X., Li, G., Zhang, W. and co-authors. 2017. Earth's changing global atmospheric energy cycle in response to climate change. *Nat. Commun.* **8**, 14367–14368. doi:10.1038/ncomms14367

Peixóto, J. P. and Oort, A. H. 1974. The annual distribution of atmospheric energy on a planetary scale. *J. Geophys. Res.* **79**, 2149–2159. doi:10.1029/JC079i015p02149

Prigogine, I. 1962. *Non-Equilibrium Statistical Mechanics*. Wiley, New York, p. 336.

Ruggieri, P., Alvarez-Castro, M. C., Athanasiadis, P., Bellucci, A., Materia, S., and co-authors. 2020. North atlantic circulation regimes and heat transport by synoptic eddies. *J. Clim.* **33**, 4769–4785. doi:10.1175/JCLI-D-19-0498.1

Salmi, T. 2002. *Detecting Trends of Annual Values of Atmospheric Pollutants by the Mann-Kendall Test and Sen's Slope Estimates-the Excel Template Application MAKESENS*. Finnish Meteorological Institute Helsinki: Ilmatieteen laitos.

Sardeshmukh, P. D. and Hoskins, B. J. 1988. The generation of global rotational flow by steady idealized tropical divergence. *J. Atmos. Sci.* **45**, 1228–1251. doi:10.1175/1520-0469(1988)045<1228:TGOGRF>2.0.CO;2

Seidel, D. J., Fu, Q., Randel, W. J. and Reichler, T. J. 2008. Widening of the tropical belt in a changing climate. *Nature Geosci.* **1**, 21–24. doi:10.1038/ngeo.2007.38

Sen, P. K. 1968. Estimates of the regression coefficient based on Kendall's tau. *J. Amer. Stat. Assoc.* **63**, 1379–1389. doi:10.1080/01621459.1968.10480934

Shaw, T. A., Barpanda, P. and Donohoe, A. 2018. A moist static energy framework for zonal-mean storm-track intensity. *J. Atmos. Sci.* **75**, 1979–1994. doi:10.1175/JAS-D-17-0183.1

Simmonds, I., Keay, K. and Lim, E.-P. 2003. Synoptic activity in the seas around antarctica. *Mon. Wea. Rev.* **131**, 272–288. doi:10.1175/1520-0493(2003)131<0272:SAITSA>2.0.CO;2

Sohn, B., Yeh, S.-W., Schmetz, J. and Song, H.-J. 2013. Observational evidences of walker circulation change over the last 30 years contrasting with gcm results. *Clim. Dyn.* **40**, 1721–1732. doi:10.1007/s00382-012-1484-z

Trenberth, K. E. and Fasullo, J. T. 2013. An apparent hiatus in global warming? *Earth's Future* **1**, 19–32. doi: https://doi.org/10.10022013EF000165, URL https://agupubs.onlinelibrary.wiley.com/doi/abs/10.1002/2013EF000165, https://agupubs.onlinelibrary.wiley.com/doi/pdf/10.1002/2013EF000165. doi:10.1002/2013EF000165

Ulbrich, U. and Speth, P. 1991. The global energy cycle of stationary and transient atmospheric waves: Results from ecmwf analyses. *Meteorl. Atmos. Phys.* **45**, 125–138. doi:10.1007/BF01029650

Veiga, J. A. P., Pezza, A. B., Ambrizzi, T., Rao, V. B., Franchito, S. H. and co-authors. 2013. The energy cycle associated to the pacific walker circulation and its relationship to enso. *Atmos. Climate. Sci.* **3**, 627–642.

Ye, Q. and Ahammed, F. 2020. Quantification of relationship between annual daily maximum temperature and annual daily maximum rainfall in south Australia. *Atmos. Oceanic Sci. Lett.* **13**, 286–288.